Determining Beta-Sheet Crystallinity in Fibrous Proteins by Thermal Analysis and Infrared Spectroscopy

Xiao Hu,[†] David Kaplan,[‡] and Peggy Cebe*[,†]

Department of Physics and Astronomy and Departments of Biomedical Engineering and Chemical and Biological Engineering, Tufts University, Medford, Massachusetts 02155

Received May 5, 2006; Revised Manuscript Received July 11, 2006

ABSTRACT: We report a study of self-assembled beta-pleated sheets in *B. mori* silk fibroin films using thermal analysis and infrared spectroscopy. *B. mori* silk fibroin may stand as an exemplar of fibrous proteins containing crystalline beta-sheets. Materials were prepared from concentrated solutions (2−5 wt % fibroin in water) and then dried to achieve a less ordered state without beta-sheets. Crystallization of beta-pleated sheets was effected either by heating the films above the glass transition temperature (T_g) and holding isothermally or by exposure to methanol. The fractions of secondary structural components including random coils, alpha-helices, beta-pleated sheets, turns, and side chains were evaluated using Fourier self-deconvolution (FSD) of the infrared absorbance spectra. The silk fibroin films were studied thermally using temperature-modulated differential scanning calorimetry (TMDSC) to obtain the reversing heat capacity. The increment of the reversing heat capacity $\Delta C_{p0}(T_g)$ at the glass transition for the less ordered, noncrystalline, silk fibroin is found to be 0.478 ± 0.005 J/(g K). As crystalline beta-sheets form, the heat capacity increment at T_g is systematically decreased. We find that the heat capacity increment from the TMDSC trace is linearly well correlated (negatively) with beta-sheet content ϕ_C determined from FSD, yielding $\Delta C_p = 0.475 - 0.494\phi_C$. The correlation allows the beta-sheet content to be determined from a direct measurement of the heat capacity increment at T_g. This type of analysis can serve as an alternative to X-ray methods and may have wide applicability to other crystalline beta-sheet forming proteins.

Introduction

Fibers from the *Bombyx mori* (domesticated) silk worm have been used for the textile industry for thousands of years. Silk fibroin, consisting of the heavy and light chains and forming the filaments of the silk fiber, is the interior structural protein which gives silk its mechanical strength, softness, and elasticity.[1,2] A water-soluble protein glue, sericin, bonds the fibroin together to form the natural silk fiber.[1] Because of its remarkable properties, silk fibroin finds application in the fields of the biomedical and biotechnological engineering, for example, in biosensors, drug release, cell adhesion and growth, tissue regeneration, and also as the potential starting material for the preparation of medical devices.[3−5] These applications are all related to the formation of the highly periodic crystalline regions in the silk fibroin.[1,6−12] *B. mori* silk fibroin stands as an exemplar of fibrous proteins containing crystalline beta-sheets.

Three structural models, termed silk I, II and III, have been reported to exist in silk fibroin. Silk I refers to the water-soluble structure existing within the silkworm gland before spinning. Silk II is the insoluble extended beta-sheet conformation which forms after the spinning of silk fibers from the spinneret of the silkworm. Silk III is an unstable structure observed at the water−air interface.[13,14] During spinning of the silk fiber, a transition occurs from silk I to silk II.[1,6] The crystallization of the beta-pleated sheets, a crystalline component formed in the some structural proteins,[15−19] was identified as the key transition to explain the process of the silk I−silk II transition.[1,6]

To obtain water-soluble silk fibroin in the laboratory, a degumming process is used to remove the sericin followed by dissolution using concentrated salt solutions, resulting in a non-beta-sheet (less ordered) state fibroin solution which can be dried to form solid less ordered, noncrystalline, silk fibroin films.[1,9,20−22] About 55% of the fibroin from a colloidal aqueous fibroin solution can be cleaved by enzymatic hydrolysis with chymotrypsin to form an insoluble crystalline powder. The remaining part of the fibroin is rich in Tyr and constitutes the less ordered part.[23−25] Exposure to organic solvents,[11,20,21] application of mechanical stress,[1,11] or thermal treatments[22,26,27] can induce nonreversible crystallization. Isothermal crystallization of regenerated *B. mori* silk fibroin results in the formation of self-assembled beta-sheets. Compared to fiber spinning from the natural silkworm gland, which produces a shear-induced crystallinity at room temperature, the non-shear-induced crystallinity of this regenerated silk biomaterial was studied in this work.

The complete sequence of the *B. mori* silk fibroin gene has been reported.[2,24] Detailed study shows 12 repeating regions along the fibroin chain are connected by 11 nonrepetitive less ordered regions in the fibroin heavy chain component. The repeating region comprised various units including the highly repetitive GAGAGS hexamer (the consensus crystalline regions) and the less repetitive GAGAGY (consensus less organized sequence) or/and AGVGYGAG motifs. The less ordered regions contain negatively charged, polar, bulky hydrophilic and aromatic amino acid residues. To understand the exact relationship involved in the formation of beta-pleated sheet structures and crystals, some simple proteins based on the silk models have been synthesized. X-ray diffraction,[28] nuclear magnetic resonance (NMR),[29,30] and Fourier transform infrared spectroscopy (FTIR)[31] have been used to analyze the effects of the different repetitive amino acid sequences on the formation of the crystals. These studies have indicated the importance of the contribution of the beta-pleated sheet structures to the crystallization of the silk fibroin.[12]

[†] Department of Physics and Astronomy.
[‡] Departments of Biomedical Engineering and Chemical and Biological Engineering.
* Corresponding author: Tel 617-627-3365; Fax 617-627-3744; e-mail peggy.cebe@tufts.edu.

10.1021/ma0610109 CCC: $33.50
Published on Web 08/11/2006

Early studies by Warwicker (1960) using X-ray diffraction analysis indicated existence of approximately 62%−65% of crystallinity in silkworm cocoon silk fibroin.[32] However, prior X-ray studies of unoriented *B. mori* silk fibroin films show that the wide-angle diffraction pattern has relatively few peaks, which are broad and weakly expressed. The peaks arise from the formation of the crystalline beta-pleated sheet secondary structures in the protein. The degree of crystallinity, calculated from the relative areas under these crystal peaks, tends to be inaccurate at low crystalline fraction.[9,33] The likely reason is that many of the crystals formed are small and imperfect. Such crystals may not contribute measurably to the overall coherent scattering in the X-ray diffraction pattern. Therefore, two other methods, infrared spectroscopy with Fourier self-deconvolution, and specific reversing heat capacity are proposed for quantification of the beta-sheet fraction.

FTIR is one of the main tools for the quantitative study of the composition in silk materials.[9,27,31,34] Previous studies on silk fibroin used direct curve fitting of the broad amide I region and contained many peaks in the fitted initial spectrum. This fitting method may produce uncertainty during the fitting process, especially for low-resolution or low-crystallinity spectra. Therefore, the method of Fourier self-deconvolution, which has been applied to other proteins[15,16,18] and is described below, is introduced for the accurate quantitative study of the beta-sheet fraction in silk fibroin.

We propose another investigative method, based on measurement of specific heat capacity increment at the glass transition, which (1) correlates with spectroscopic methods such as FTIR, (2) quantifies the beta-pleated sheet fractions including in cases where other methods, such as X-ray or FTIR, cannot be used, and (3) can serve as a standard method to assess the beta-pleated sheet fraction in this and other fibrous proteins. This method is well-known in the study of synthetic semicrystalline polymers[35−40] and has been used by our group[41−45] to determine the fraction of the material, in semicrystalline polymers called the "mobile amorphous fraction", which can exhibit its glass transition relaxation process during heating.[35−40] In the present study we compare the results of the heat capacity measurements to the beta-pleated sheet content assessed by Fourier self-deconvolution of the FTIR spectrum in the amide I region (1600−1700 cm^{-1}). We find a strong (negative) correlation between the mobile fraction from heat capacity measurements at T_g and the beta-pleated sheet fraction from FTIR. The thermal method can thus serve as an alternative to X-ray methods for determining the beta-sheet content and may have wide applicability to other semicrystalline proteins.

Theoretical Basis

In this work we apply temperature-modulated differential scanning calorimetry (TMDSC) for the first time to study the heat capacity of *B. mori* silk fibroin. Thermal analysis for the study of heat capacities of globular proteins has been reported.[46] This allows a careful determination of the specific reversing heat capacity in the vicinity of the glass transition temperature (which is 178 °C for silk fibroin[7,22,26]). In TMDSC the time dependence of sample temperature is written as[47]

$$T(t) = T_0 + qt + A\sin(\omega t - \theta) \tag{1}$$

where T_0 is the initial temperature, q is the linear heating rate, A is the amplitude of temperature oscillation, ω is the modulation frequency, and θ is the phase shift with respect to the reference. In TMDSC we measure the "reversing heat capacity," a term defined in TMDSC to represent a heat effect which can be reversed within the temperature range of the modulation[47] and calculated from[48−50]

$$|mC_p + C_s - C_r \pm \Delta C_{cell}| = (A_T/A)[(K/\omega)^2 + C_r^2]^{1/2} \tag{2a}$$

$$= K'(A_{HF})/A \tag{2b}$$

where mC_p is the heat capacity of a sample of mass, m, and specific heat capacity, C_p; C_s is heat capacity of the sample pan, and C_r is the heat capacity of an empty reference pan; ΔC_{cell} is the cell asymmetry correction which can be determined by running a series of empty pans with various mass differences compared to the reference.[43,50] On the right-hand side of eq 2, A_T is the amplitude of temperature difference between sample and reference; A is the sample temperature modulation amplitude; K is Newton's law calibration constant which is independent of modulation frequency and reference; A_{HF} is the heat flow amplitude, and K' is a calibration constant at each individual temperature provided the same experimental conditions are maintained to ensure the same heat transfer (e.g., same reference, same modulation frequency).

From a standard DSC measurement with a constant applied heating rate we obtain the total heat capacity, which consists of both the reversing and nonreversing components, from

$$mC_p = K''HF/q \tag{3}$$

where K'' is a calibration constant and HF is heat flow. If the heat capacity is reversing, eqs 2 and 3 give the same result; if not, the difference between eqs 3 and 2 gives the nonreversing heat capacity component. The reversing heat effect in *B. mori* silk fibroin was obtained from below the glass transition to just below the thermal degradation temperature. The use of the reversing heat capacity to determine the mobile fraction will be presented in the Results section.

In addition to thermal analysis, we used infrared spectroscopy to study *B. mori* silk fibroin. Fourier self-deconvolution (FSD) is a signal-processing tool for infrared spectral analysis that allows resolution of a band contour comprising several overlapped bands.[51−54] Using a high pass filter, the broad and indistinct bands, such as the amide I region of protein spectra, can be narrowed synthetically to provide a deconvoluted spectrum with better peak resolution.

The general procedure applied to a single band, following the method of Lorenz-Fonfria,[54] is to consider the experimental spectrum, $E(\nu)$ (where ν is the wavenumber), as a general convolution of a narrow Dirac delta-function band, having area A located with the center of the band at ν_0, with two spreading functions. The band spreading functions include the band shape function $L(\nu)$, which broadens the band homogeneously and inhomogeneously, and an instrumental broadening function, $R(\nu)$. This convolution is written (with convolution operator, $\otimes$) as[54]

$$E(\nu) = A\delta(\nu - \nu_0) \otimes L(\nu) \otimes R(\nu) \tag{4}$$

If the instrumental broadening is insignificant with respect to $L(\nu)$, then the band will be narrowed by simply deconvoluting $L(\nu)$.

To deconvolute $L(\nu)$, we take advantage of the fact that the interferogram, $I(x)$, is related to the experimental spectrum through $E(\nu) = \mathcal{F}\{I(x)\}$ and $I(x) = \mathcal{F}^{-1}\{E(\nu)\}$, where $\mathcal{F}$ represents Fourier transformation and $\mathcal{F}^{-1}$ represents the reverse Fourier transform. Then the convolution theorem is used to write $I(x)$ as

$$I(x) = \mathcal{F}^{-1}\{A\delta(\nu - \nu_0) \otimes L(\nu) \otimes R(\nu)\} = \mathcal{F}^{-1}\{A\delta(\nu - \nu_0)\}\mathcal{F}^{-1}\{L(\nu)\}\mathcal{F}^{-1}\{R(\nu)\} \quad (5)$$

$$I(x) = \mathcal{F}^{-1}\{A\delta(\nu - \nu_0)\}L(x)\,R(x) \quad (6)$$

The Fourier conjugate function $R(x) = \mathcal{F}^{-1}\{R(\nu)\}$ is selected using an apodization function; $L(x) = \mathcal{F}^{-1}\{L(\nu)\}$ is typically a Lorentzian function. Resolution enhancement of the FSD spectrum, $E'(\nu)$, is obtained by dividing $I(x)$ by $L(x)$ and Fourier transforming the result. This process is now included as part of the analysis software of most commercial FTIR spectrometers.

FSD has been applied to the study of secondary structures of proteins either in solution[18] or as thin films[15] by analyzing the amide I (1600−1700 cm^{-1}) vibrational modes. The conformation-sensitive amide I region results mainly from the overlapping of the stretching vibrations of pure C═O bonds (80%) in the protein backbones, which is often free of the other bands. The frequency of these vibrations is determined from the nature of the hydrogen bonds involved in the carbonyl groups, which directly relate to the particular secondary structure.[16] Coleman et al. showed for nylons that the conformationally sensitive amide I region could be conveniently used for quantitative FTIR analysis because the absorptivity coefficients of the constituent hydrogen-bonded carbonyl groups did not differ appreciably.[55−57]

Mouro et al.[18] evaluated the amide I region of camphor-bound cytochrome P-450 and estimated the fractions of α-helix, β-sheet, and turns structures by FSD, which fractions compared favorably to crystallographic data. Goormaghtigh et al.[15] applied FSD to thin hydrated films of 17 membrane proteins. They estimated the fractions of α-helix, β-sheets, random coils, and β-turns structures and compared the results to X-ray data. They concluded that the FSD method provided correct estimation of the secondary structures of these proteins. Jung[16] provides an excellent overview of the use of FTIR, including deconvolution, for structure determination emphasizing heme-type proteins, especially cytochrome P450. The previous work[15,16,18,51−57] gives us a solid theoretical and experimental foundation to use this powerful tool for the quantitative study of secondary structure in the silk fibroin film.

Experimental Section

Materials and Preparation. Cocoons of *B. mori* silkworm silk (obtained from Tsukuba, Japan) were boiled for 25 min in an aqueous solution of 0.02 M Na_2CO_3 and rinsed thoroughly with water to extract the gluelike sericin.[1] The remaining silk fibroin was dissolved in a 9.3 M LiBr solution at 60 °C for 4−6 h and then dialyzed in distilled water using a Slide-a-Lyzer dialysis cassette (Pierce, MWCO 3500) for 2 days. After centrifugation and filtration to remove insoluble residues, the final 2−5 wt % silk fibroin aqueous solution was cast in polystyrene Petri dishes to make silk fibroin films. After drying to remove water, the resulting dry film thickness is around 60 μm. The fibroin films were then put into a vacuum oven at room temperature for 3−4 days to remove moisture on their surfaces. To avoid the effects of water on the crystallization of silk fibroin,[26] before every experiment, the samples were always first put into a Mettler hot stage (FP90) and then slowly heated (at heating rate of ∼2 °C/min) to 165 °C, which is below the glass transition temperature reported for silk fibroin, T_g = 178 °C.[7,22] The films were kept isothermally for 30 min to remove water; efficacy of the water removal procedure was checked by Fourier transform infrared attenuated total reflectance (FTIR-ATR) measurement (details of FTIR are given below). The dried films were moved to the differential scanning calorimeter (DSC) for the isothermal crystallization study.

The films were completely noncrystalline prior to the crystallization procedure. Here we will use the terms "less ordered" and "noncrystalline" to represent all elements of the secondary protein structure that are not the crystalline beta-pleated sheets, including all turns, random coils, alpha-helices, extended chains, and side chains. Only the crystalline beta-sheets contribute to the coherent wide-angle X-ray scattering peaks. Prior to crystallization there was no signature of beta-pleated sheets in either the FTIR absorption spectrum or the WAXS diffractogram. The dried less ordered, noncrystalline films rapidly and completely dissolved when placed in room temperature water, whereas semicrystalline films, containing insoluble beta-pleated sheets,[1] did not. For comparison to the thermally crystallized samples, several films were subjected to methanol exposure, a treatment known to induce formation of crystalline beta-sheets.[20,21]

Thermal Analysis. The samples with mass about 8 mg were encapsulated into Al pans and heated in a TA Instruments 2920 DSC, which was purged with a dry nitrogen gas flow of 30 mL/min. The instrument was calibrated for empty cell baseline and with indium for heat flow and temperature. The silk fibroin was treated using "cold" crystallization; i.e., the less ordered, noncrystalline films were heated to a temperature above the glass transition temperature, at which point the molecules gain sufficient mobility for crystalline beta-pleated sheets to form.

Standard mode DSC measurements were performed at a heating rate of 2 °C/min from room temperature to the isothermal crystallization temperature, T_c. T_c ranged from 192 to 214 °C for DSC studies. Samples were maintained at T_c for a certain time (less than about 250−300 min) until crystallization was completed and no more exothermic heat flow could be observed at this temperature. The samples were then cooled and reheated using temperature-modulated DSC (TMDSC). The glass transition was determined from the midpoint of the step in the reversing heat capacity.

TMDSC measurements were performed using a TA Instruments Q100 (or 2920), equipped with a refrigerated cooling system (or liquid nitrogen cooling accessory). The less ordered (noncrystalline) and isothermally crystallized samples were heated at 2 °C/min from room temperature to the beginning of the degradation temperature (∼230 °C[7,22]), with a modulation period of 60 s and temperature amplitude of 0.318 °C. Aluminum and sapphire reference standards were used for calibration of the heat capacity. TMDSC endotherms are presented with downward deflection from the baseline. All the sample pans were weighed again after the experiment, and the new weight (always within 3% of the original weight) was used for determination of the specific heat capacity.

The reversing heat capacity measurement consisted of three runs, as described in our earlier work.[43] The first run is empty Al sample pan vs empty Al reference pan to obtain the cell asymmetry and baseline correction. The second run is sapphire standard vs empty Al reference pan to calibrate heat flow amplitude according to standard equations, published previously.[43,48,50] The third run is sample vs empty Al reference pan. The same empty Al reference pan was used in all the runs, and all the Al sample pans were kept the same in weight.

FTIR Analysis. Prior to FTIR analysis, the film samples were heated to different crystallization temperatures in either the Mettler FP90 hotstage or the DSC and held until isothermal crystallization was completed. FTIR analysis of treated samples was performed in a Bruker Equinox 55/S FTIR spectrometer, equipped with a deuterated triglycine sulfate detector and a multiple-reflection, horizontal MIRacle ATR attachment (using a Ge crystal, from Pike Tech.). The instrument was continuously purged by nitrogen using blow-off from a liquid nitrogen tank to eliminate the spectral contributions of atmospheric water vapor. For each measurement, 128 scans were coadded with resolution 4 cm^{-1}, and the wavenumber ranged from 400 to 4000 cm^{-1}.

Fourier self-deconvolution (FSD) of the infrared spectra covering the amide I region (1595−1705 cm^{-1}) was performed by Opus 5.0 software. The second derivative was first applied to the original spectra in the amide I region with a nine-point Savitsky-Golay smoothing filter. Deconvolution was performed using Lorentzian

line shape with a half-bandwidth of 25 cm^{-1} and a noise reduction factor of 0.3 (the fraction of the interferogram to which the combination of the deconvolution and apodization is applied). Apodization with a Blackman-Harris function was always performed automatically at the same time in the software.

The parameters were chosen on the basis of the resolution and the band position of the deconvoluted spectra. The positions (in cm^{-1}) of the band maxima in the deconvoluted spectra were made to correspond to the frequency of the minima in the second derivative of the undeconvoluted spectra. The deconvoluted spectra is better suited for subsequent curve fitting,[52,53] for example, by keeping the position of the bands stable when using the autofit program in the software and by separating the amide I region from the total deconvoluted spectra for making baseline correction. A straight baseline passing through the deconvoluted amide I spectra was subtracted. A baseline correction using the Bezier function was also made on the left and right sides of the deconvoluted amide I region.

To measure the relative areas of the amide I components, FSD spectra were then curve-fitted. The decomposition method assumes that the extinction coefficient for the C═O stretch vibration is same for the different structural components. Thus, band intensities are proportional to the fraction of each secondary structural component. The number and position (in cm^{-1}) of the fitted bands were taken from the smoothed second derivative of the original spectra. The contribution of silk fibroin amino acid side chain absorption was not removed from the amide I initial spectra and will be discussed later on in the Results section.

Gaussian line shape profiles were used in the fit although the Voigt function (a convolution of Lorentzian and Gaussian functions) can also be used. Comparison of the fitting results shows that these two peak functions yield almost the same results in this study, and the Lorentzian contribution to the band shape of the Voigt function was always less than 10% for the few non-100%-Gaussion contributed Voigt peaks after using autofit in the software. The curve fitting proceeded as follows: (i) The initial band positions were fixed first, using a fixed number of the bands, but allowing their widths and heights to vary. (ii) The band positions were then allowed to change within a limited region by using the Levenberg−Marquardt algorithm. (iii) A nonlinear least-squares method was finally used to make the reconstituted overall curve as close as possible to the original deconvoluted spectra. The fitting results were further evaluated by examining the residual from the difference between the fitted curve and the original curve.

Finally, the deconvoluted amide I spectra were area-normalized. The relative areas of the single bands were used to determine the fraction of the secondary structural elements. To avoid possible artifacts arising from the deconvolution step, we chose different FSD factors (i.e., half-bandwidth = 15, 20, 30 cm^{-1} and noise reduction factor = 0.2, 0.4) for each spectrum. To evaluate the impact of different choice of FSD factors, we fitted the deconvoluted spectra, using the curve-fitting procedure above. Results showed very little difference for the fractions of the secondary structures, and the variation is covered over by the error bars (or symbols) in our figures.

Results and Discussion

Determination of Beta-Sheet Content by Fourier Transform Infrared Spectroscopy. Figure 1 shows the original FTIR spectra in the amide I region for eight samples, including the less ordered (noncrystalline) sample (curve 1), samples crystallized at 192, 195, 199, 204, 209, and 214 °C (curves 2−7, respectively), and a four-day methanol-treated sample (curve 8). The assignment of the vibrational bands is made by reference to the literature and will be discussed below. Table 1 lists the wavenumber ranges corresponding to vibrational bands in *B. mori* silk, within the amide I region of the spectrum, along with the literature references. The original absorption curves are displaced vertically but are similarly scaled. The dashed line marks the center of the absorption band at 1625 cm^{-1}, characteristic of antiparallel beta-sheets (see Table 1), and this band strengthens as crystallization temperature increases. The random coil band at 1647−1655 cm^{-1} simultaneously diminishes.

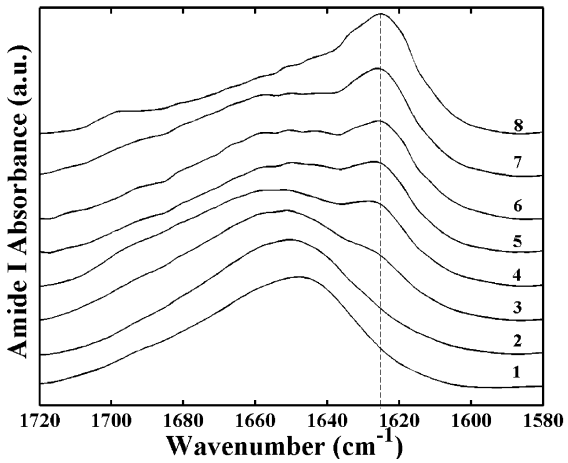

Figure 1. Experimentally determined FTIR absorbance spectra in the amide I region vs wavenumber for *B. mori* silk fibroin. Less ordered, noncrystalline sample (curve 1), samples crystallized at 192, 195, 199, 204, 209, and 214 °C (curves 2−7, respectively), and a four-day methanol-treated sample (curve 8).

Table 1. Vibrational Band Assignments in the Amide I Region for *B. Mori* Silk Fibroin

wavenumber range, cm^{-1}	assignment	reference
1605−1615	(Tyr) side chains/aggregated strands	16, 18, 34, 58
1616−1621	aggregate beta-strand/ beta-sheets (weak)[a]	27, 31, 58
1622−1627	beta-sheets (strong)[a]	15−18, 59
1628−1637	beta-sheets (strong)[b]	15−18, 27, 31, 34, 52, 58
1638−1646	random coils/extended chains	15, 27, 31, 34, 58
1647−1655	random coils	27, 34
1656−1662	alpha-helices	27, 34
1663−1670	turns	16−18, 27, 31, 60
1671−1685	turns	16−18, 27, 31, 60
1686−1696	turns	16−18, 27, 31, 60
1697−1703	beta-sheets (weak)[a]	27, 31, 34, 20, 21

[a] Intermolecular beta-sheets. [b] Intramolecular beta-sheets.

The amide I band was deconvoluted to determine the fraction of the beta-sheets formed during crystallization using the method of Fourier self-deconvolution (FSD).[51−54] In this approach, the broad and typically indistinct amide I band is transformed to yield a fitted self-deconvoluted set of bands from amide I′ (prime refers to the resultant spectrum), from which the secondary structural elements are determined.[15,16,18] In our study, the computer-imitated total side chains absorption was not subtracted from the original spectrum in the amide I and II region. This is due to their extremely low intensity compared to the original spectrum for the silk fibroin and their narrow contribution in the amide I region (around 1600−1620 cm^{-1}) compared to other proteins.[18,19] Therefore, the side chains absorption of the silk fibroin have not broadly mixed with other bands in the amide I region, and we can easily separate them from other components by fitting the Fourier self-deconvoluted original spectra. Figure 2 shows the fitted spectra of less ordered noncrystalline sample (Figure 2a), sample thermally treated at 204 °C (Figure 2b), and methanol-treated sample (Figure 2c). The solid heavy curve is the resultant amide I′ spectrum, and the lighter dotted curves are the individual deconvoluted peaks.

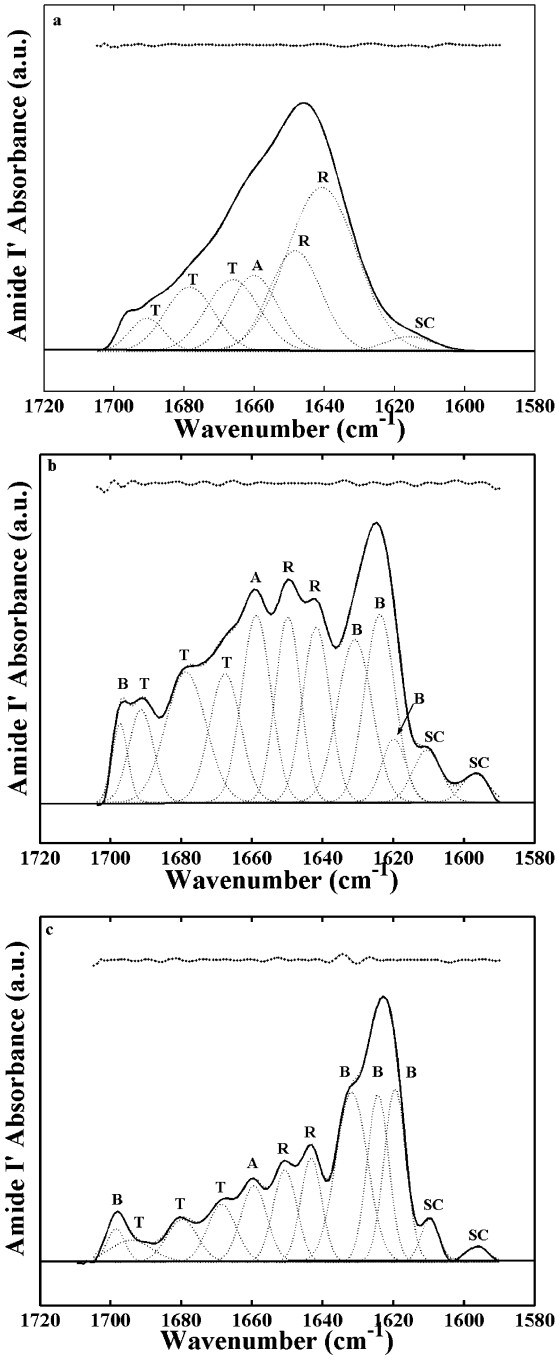

Figure 2. Absorbance spectra, amide I′, deduced after Fourier self-deconvolution. The heavy line represents the deduced absorbance band. The light lines represent the contributions to the amide I′ band and are marked as random coil (R), beta-sheets (B), alpha-helices (A), turns (T), and side chains (SC). The dotted line is the summation of the individual contributions, and the residue between the deduced absorbance and the summation is indicated above the spectra. (a) Random coil sample; (b) sample isothermally crystallized at 204 °C; (c) sample crystallized by four-day exposure to methanol.

The peaks are marked with abbreviations that stand for turns (T), alpha-helix (A), random coil (R), beta-sheets (B), and side chains (SC). At the top of Figure 2a−c, the dotted line represents the residue between the fitted curve and the summation of the deconvoluted Gaussian component curves.

The assignment of the amide I region bands was determined by reference to the literature. The band between 1605 and 1615 cm^{-1} (centered around 1611 cm^{-1} in Figure 2a−c and marked SC) comes from the side chains or aggregated strands.[16,18,34,58] This absorption peak may be related to the side chains of Tyr for the H_2O-based protein samples,[61] known to exist in *B. mori* fibroin at about 4.8%.[1] Arg side chains may also contribute to this band[61] but will not contribute strongly to the absorption due to the very small fraction (0.5%) in *B. mori* fibroin film.[1] This side chain can be seen in both crystallized samples (Figure 2b,c) and the less ordered sample (Figure 2a) and is usually next to another side-chain band (centered around 1597 cm^{-1} in Figure 2b,c and also marked SC) located within the amide II region (1450−1600 cm^{-1}). The band between 1616 and 1621 cm^{-1} (centered around 1619 cm^{-1} in Figure 2b,c and marked B) is usually assigned to the intermolecular beta-sheet formation and molecular aggregation.[27,31,58] Analysis of the second-derivative spectrum shows that this band increases during the isothermal crystallization whereas the side-chain bands remain stable. As shown in Figure 2b, this intermolecular beta-sheet band sometimes merges together with the next very intense band (located at 1622−1627 cm^{-1} in Figure 2b,c and also marked B), which can occur if we choose either a small FSD Lorentzian half-width or a higher noise reduction factor. However, the total change caused by this band combination will only be ±2% to the total amount of beta-sheets.

The band between 1622 and 1627 cm^{-1} (centered around 1624 cm^{-1} in Figure 2b,c and marked B) is a well-known intermolecular beta-sheet band existing in most crystallized proteins.[15−18,59] The previous studies in silk fibroin shows that this is a type of stacked antiparallel beta-sheets structure.[20,21,27,31,60] The structural model of this polypeptide crystal has been well-defined in previous studies.[28] The band between 1628 and 1637 cm^{-1} (centered around 1630 cm^{-1} in Figure 2b,c and marked B) is due to the formation of the intramolecular beta-sheets.[15−18,27,31,34,52,58] The analysis of the silk fibroin peptide sequence GAGAGS/GY∼GY suggests that it can form 12 intramolecular antiparallel beta-strands with 11 turns of type GT∼GT, in one heavy chain molecule of the silk fibroin.[2] It should be pointed out that some proteins may also contain this band in the less ordered state, which most authors believe comes from a beta-sheet-like structure with hydrogen bonding to another type of structure,[62] or to nonbonded beta-sheets,[63] or to irregular pieces of extended chain structures similar to the beta-sheets.[64] The same band was also found in the biosynthesized silk I structure[31] which was used as a model in NMR studies[29] to substitute for the less ordered (noncrystalline) silk fibroin.

In our study, when we examined the thicker part right on the edge of our cast less ordered film, we found a tiny band centered around 1630 cm^{-1} (observed from FTIR second-derivative spectrum), which contributes an amount less than 4% to the total amide I region. In the central thinner part of our cast less ordered noncrystalline films, this band was absent. The presence of this tiny band in an otherwise less ordered sample may indicate that there can be some primary noncrystal folding structure within a single molecular chain prior to crystallization. Further studies are underway to clarify this point.

Another factor that needs to be considered is that H_2O can also form a band around 1636 cm^{-1}.[59] Our silk fibroin films usually contain about 5% H_2O immediately after film-casting and were annealed at 165 °C specifically to remove water. FTIR examination shows that there was no effect of water in the dried less ordered solid-state samples before crystallization.

In Figure 1, the three beta-sheet bands assigned above (in the region from 1617 to 1637 cm^{-1}) generate the intense peak in the amide I region (centered at the dotted vertical line). Another small beta-sheet band was observed at the high end of

the amide I region between 1697 and 1703 cm^{-1}.[27,31,34] In our work, the intensity of this band increased in parallel with the formation of the dominant 1617−1637 cm^{-1} beta-sheets peak during thermal crystallization. Other work[20,21] on silk fibroin crystallized by solvent-exposure confirms that the band at 1697−1703 cm^{-1} intensifies with crystallization. The area fraction of the fitted peak from this band was normally smaller than 4% of the total amide I region.

Between the major beta-sheet triplet of bands at 1617−1637 cm^{-1} and the minor beta-sheet band at 1697−1703 cm^{-1} are several bands attributed to random coils, alpha-helices, and turns structure (see Table 1). The band between 1638 and 1646 cm^{-1} (centered around 1640 cm^{-1} in Figure 2a and marked R) was assigned to random coils with extend chains in solid-state films.[15,27,31,34,58] The next two close bands, between 1647 and 1655 cm^{-1} (centered around 1650 cm^{-1} in Figure 2a and marked R) and between 1656 and 1662 cm^{-1} (centered around 1659 cm^{-1} in Figure 2a and marked A) were assigned to another random coil band and a band from alpha-helix structures, respectively.[27,34] From FSD and the analysis of the second-derivative spectrum, these three bands all decrease during crystallization. The 1656−1662 cm^{-1} alpha-helix band decreased more slowly than the random coil bands at 1647−1655 and 1638−1646 cm^{-1}, and after the crystallization the center of the random coil band at 1638−1646 cm^{-1} shifted to slightly higher wavenumber, from 1639 to 1642 cm^{-1}.

The next three bands in Figure 2a−c, 1663−1670 cm^{-1} (centered around 1666 cm^{-1}), 1671−1685 cm^{-1} (centered around 1680 cm^{-1}), and 1686−1696 cm^{-1} (centered around 1691 cm^{-1}), are assigned to the turns structure.[16−18,27,31,60] Analysis of the second-derivative spectrum in this region shows that there might be a very tiny band between 1672 and 1677 cm^{-1} in the turns region, which only can be observed when we use very high FSD Lorentzian half-width (>50) with small noise reduction in the FSD. This tiny band can still be assigned to turns structure,[17,27] but sometimes it is treated as a extremely weak beta-sheet band.[31,60] We compared the difference between adding and omitting this band peak in the process of FSD curve fitting. Results show that this tiny peak will contribute a maximum of 2% to the total area of the amide I region, a difference covered by the error bars in the calculation of the beta-sheet fraction.

Therefore, we chose to use 11 peaks (centered around 1611, 1619, 1624, 1630, 1640, 1650, 1659, 1666, 1680, 1691, and 1698 cm^{-1}) to fit the FSD amide I region of the crystallized samples, according to the resolution of the FSD curves and the band assignments described above. Figure 2a−c shows examples of the Gaussian curve fitting (dotted curves) of the amide I′ region (solid curve) for three samples.

The ratio of the individual peak area to the total amide I′ band area was determined and serves to quantify the amount of the secondary structural elements in *B. mori* silk fibroin. Similar deconvolution was carried out for all crystalline samples. Figure 3 illustrates the fractions of beta-sheets (solid circles), random coils/alpha-helices summed together (open circles), turns (triangles), and side chains (diamonds) as a function of the crystallization temperature. On the left-hand side of Figure 3, the fractions of secondary structures in the less ordered sample are shown. On the right-hand side, the fractions of secondary structures in the 1−4 days methanol-treated samples are shown. For these two regions, the *x*-axis temperature scaling does not apply. These samples are included for comparison only. The accuracy in the beta-sheet fraction determined from FSD is ±1%.

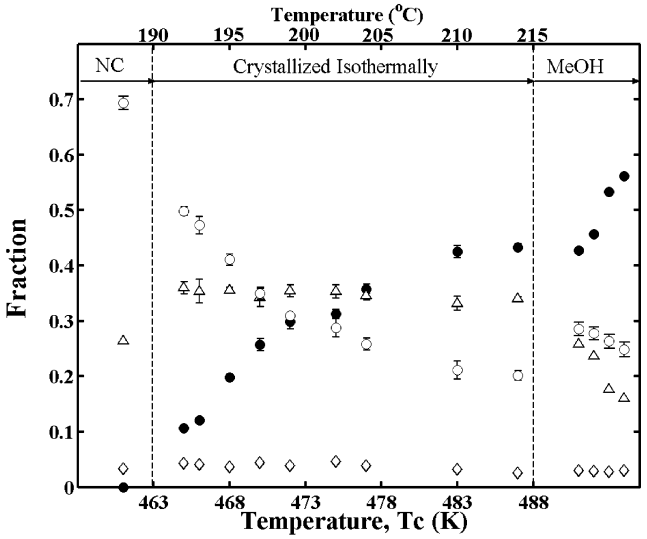

Figure 3. Fractional contributions to the FTIR amide I absorbance spectrum, determined by Fourier transform self-deconvolution, vs crystallization temperature for *B. mori* silk fibroin. Random coils and alpha-helices summed together, open circles; beta-sheets, filled circles; turns, triangles; side chains, diamonds. The vertical dashed lines separate the noncrystalline sample on the left side and the methanol-treated samples on the right side. These data are included for comparison only, and the horizontal temperature axis does not apply to these samples.

In Figure 3, we see that as the isothermal crystallization temperature increases, the side-chain fraction (diamonds) in amide I remains stable, at about 2.5−4%. The turns structure (triangles) is also almost stable, within the limits of the errors bars on the measurement. The random coil/alpha-helix fraction (open circles) decreases with increasing T_c. The fraction of beta-sheet (solid circles) increases with increasing T_c, suggesting that this is the only crystal structure formed during isothermal crystallization above the glass transition. These results are similar to those of Coleman et al., who studied hydrogen bonding in polyamides and polyurethanes.[55−57] In their work, three carbonyl groups (called "disordered", "ordered", and "free") were established to describe the amide I region. In *B. mori* silk fibroin, the random coils and alpha-helices can be associated with the disordered hydrogen-bonded carbonyl groups in Coleman's study. The beta-pleated sheets are associated with the ordered hydrogen-bonded carbonyl groups. Both the random coils/alpha-helices and beta-sheets change during the thermal crystallization (see Figure 3), as was found by Coleman when nylon crystallized. The "free" carbonyl groups, which remained almost stable up to the melting point in Coleman's study, are very similar to the turns structures in *B. mori* silk fibroin which we found to be relatively insensitive to thermal treatment.

Four different methanol-treated samples were studied for comparison, and these are shown on the right-hand side of Figure 3. Here, the exposure time to methanol was variable, resulting in different fractions of the secondary structures. The side-chain fraction is stable and has the same value among all samples studied, whether less ordered or crystalline. The random coil/alpha-helix structures have decreased slightly with the longer solvent treatment time, while the turns structure has decreased significantly. At the same time that the turns structure is decreasing, the beta-sheet fraction is increasing, ultimately causing a large increase in the fraction of the beta-pleated sheet for solvent-induced crystallization compared with the thermal crystallization.

In a recent study by NMR,[30,65] it was suggested that the beta-helix or distorted beta-turn structures may exist as an intermedi-

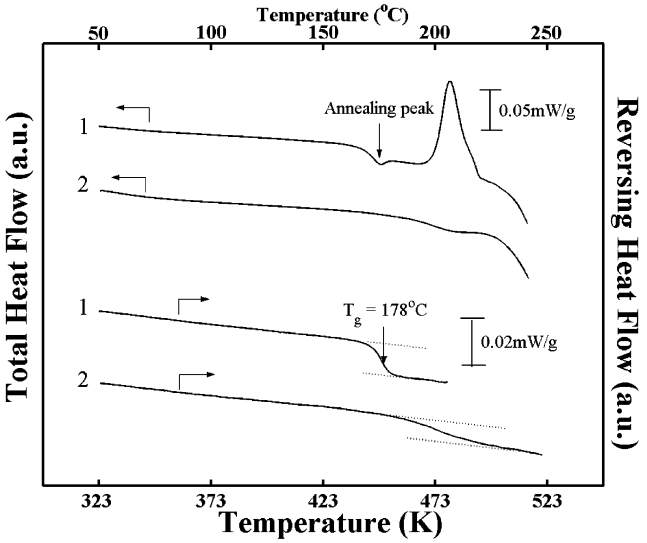

Figure 4. Heat flow vs temperature during TMDSC scanning of *B. mori* silk fibroin at 2 °C/min. Left hand axis: total heat flow. Right-hand axis: reversing heat flow. The dashed tangent lines in the reversing heat flow curves indicate the step change occurring at the glass transition temperature. Curve 1, noncrystalline sample; curve 2, sample crystallized by exposure to methanol.

ate during the formation of the silk fibroin crystal. These results provide an explanation for our observation of decrease in turns and simultaneous increase in beta-sheet fraction; that is, the turns structure can relax and transform to the beta-sheet bands region during solvent-induced crystallization. The beta-helix, unfortunately, cannot be identified easily by FTIR techniques.[66] However, it is clear that normal turns structure cannot form the crystalline region, as has been discussed within the context of the silk fibroin heavy chain model.[2] Therefore, we can conclude that only the four beta-sheet bands we assigned above can contribute to the crystals formed during the crystallization (no matter whether the crystallization is induced thermally or by solvent exposure). So their total summed peak fractions in the amide I region can stand for the crystallinity of the silk fibroin and can then be used to compare with the crystallinity value of silk fibroin obtained by other experimental methods. In fact, this method has been widely used for the comparison of crystallinity values between FTIR data and X-ray data in many other protein structures.[15,17]

An Alternative Method for Determination of the Fraction of Beta-Sheets. TMDSC was used for the first time to study the absolute crystallinity of *B. mori* silk after beta-sheet crystallization at different temperatures. Figure 4 shows the TMDSC total heat flow (left-hand axis) and reversing heat flow (right-hand axis) as a function of temperature of a less ordered noncrystalline film (curve 1) and a film crystallized by exposure to methanol for 4 days (curve 2). The reversing heat flow of less ordered film shows a step change at the glass transition, near 178 °C. For the methanol-treated sample, due to beta-sheet crystallization, the reversing heat flow step diminishes and T_g moves to a higher temperature, close to 202 °C.

The total heat flow trace of the less ordered film show a tiny endothermal peak (downward deflection from the baseline) found at the location of the glass transition. This peak is due to the previous 165 °C annealing done to remove trace water and does not affect the step height of the reversing heat flow trace at T_g. Above the temperature of the glass transition step (seen in the reversing heat flow trace at 178 °C), the total heat flow shows a large exothermic peak centered at about 213 °C from beta-sheets crystallizing nonisothermally during the scan. The methanol-treated film does not crystallize any more during the scan. For both samples, the total heat flow decreases at the highest temperatures due to onset of thermal degradation. There was no melting endotherm observed in any samples. Silk fibroin degrades at a temperature lower than the crystal melting point.

Changes in the reversing heat capacity increment at the glass transition temperature, $\Delta C_p(T_g)$, were used to determine the quantity of crystalline beta-pleated sheets formed after isothermal crystallization. First, to obtain the change of heat capacity for the 100% noncrystalline silk fibroin film, ΔC_{p0}, films were cast at room temperature from different concentrated solutions (2−5%). FTIR, X-ray diffraction, and complete solubility in water were used to confirm that no beta-sheet crystals had been formed, verifying that these films are in the completely less ordered noncrystalline state. After repeated TMDSC runs on different samples, the average value for heat capacity increment of less ordered silk fibroin was determined to be $\Delta C_{p0}(T_g) = 0.478 \pm 0.005$ J/(g K).

Next, initially less ordered silk fibroin films were heated inside the DSC to the isothermal crystallization temperature, for T_c in the range from 192 to 214 °C, and held until crystallization of beta-sheets was completed. The films were cooled to room temperature and reheated to obtain the specific reversing heat capacity traces. Figure 5a shows the specific reversing heat capacity in the vicinity of the glass transition for a less ordered sample and for samples crystallized at different temperatures. The inset in Figure 5a shows the heat capacity over the complete temperature range for a single less ordered noncrystalline sample.

The glass transition step can be seen to reach a plateau at higher temperatures. With an increase of the crystallization temperature, the specific reversing heat capacity of the high-temperature plateau decreases, and the glass transition temperature itself increases. The beta-pleated sheet crystals perform a similar role in silk fibroin that lamellar crystals do in semicrystalline synthetic polymers. That is, the beta-sheets act as physical cross-links, causing a broadening of the relaxation process at T_g and a shift of T_g to higher temperatures due to restrictions on the mobility of the remaining less ordered segments.[35−45] The reduction in the specific reversing heat capacity increment occurs because of (1) formation of beta-sheets which reduces the mass fraction of less ordered, and mobile, chain segments available to participate in the glass transition process and (2) possible formation of highly constrained, immobilized noncrystalline segments which also do not contribute to the heat capacity increment at T_g. In *B. mori* silk fibroin, the latter would play the same role that the "rigid amorphous fraction" does in semicrystalline synthetic polymers.[35−45]

Figure 5b sketches the method used to determine the heat capacity increment for the less ordered sample (dotted curve), ΔC_{p0}, and for the semicrystalline sample containing beta-sheets (light solid curve), ΔC_p^{SC}. The heavy lines represent the extrapolations of the tangents to the specific reversing heat capacity curves. The tangent from below T_g gives the solid state heat capacity, $C_p(T)^{solid}$, which is dominated by vibrational modes. Below T_g of the noncrystalline sample, we evaluated the specific heat capacity of the solid state and found $C_p(T)^{solid} = 0.130 + 3.70 \times 10^{-3}T$ [J/(g K)] with correlation coefficient of 0.992 (average of three runs, from 310 to 440 K). The accuracy in the heat capacity is ±1.5%.

The tangent above T_g gives either the liquid heat capacity, $C_p(T)^{liquid}$, for the less ordered noncrystalline sample or the semicrystalline heat capacity, $C_p(T)^{SC}$, for sample containing

Table 2. Heat Capacity Increment[a] and Mobile (M), Rigid, and Beta-Sheet (C) Fractions in *B. Mori* Silk Fibroin as a Function of Treatment

T_c (°C)	ΔC_p (J/(g K)) ± 0.01	ϕ_M[b] ± 0.02	ϕ_{RIGID}[c] ± 0.02	ϕ_C[d] ± 0.01
noncrystalline[e]	0.478 ± 0.005	1.00	0	0
192	0.41[9]	0.88	0.12	0.11
193	0.41[1]	0.87	0.13	0.12
195	0.38[4]	0.81	0.19	0.18
195	0.36[6]	0.77	0.23	0.20
197	0.34[2]	0.72	0.28	0.26
199	0.34[5]	0.73	0.27	0.30
202	0.31[5]	0.66	0.34	0.31
204	0.30[4]	0.64	0.36	0.36
209	0.24[9]	0.52	0.48	0.43
214	0.25[7]	0.54	0.46	0.43
MeOH[f]	0.27[3]	0.57	0.43	0.43
MeOH[f]	0.27[6]	0.58	0.42	0.46
MeOH[f]	0.21[3]	0.45	0.55	0.53
MeOH[f]	0.19[6]	0.41	0.59	0.56

[a] Data for crystalline samples are significant in the second digit. The third digit is included only to show the range of values. [b] Determined from thermal analysis using eq 8. [c] Determined from eq 7a. [d] Determined from FTIR analysis of the amide I region using FSD. [e] Data represent the average of four samples. [f] Samples treated for 1−4 days in methanol at room temperature.

beta-sheets. The upper and lower temperature tangents are extrapolated to the glass transition temperature (here, we used the midpoint of the sigmoidal heat capacity step), and the ΔC_p is calculated as the difference between the specific reversing heat capacity tangent values at T_g.[35−45]

For the purposes of thermal analysis of the heat capacity, by analogy to semicrystalline synthetic polymers, silk fibroin films will be modeled as comprising three fractions, viz., the mobile fraction, ϕ_M, the crystalline beta-sheet fraction, ϕ_C, and the immobilized noncrystalline fraction, ϕ_{IMM}. The fraction ϕ_{IMM} includes any immobilized noncrystalline portions of the silk fibroin that remain solidlike above the glass transition of the mobile fraction. Together, the beta-sheet crystals and the immobilized fraction constitute the rigid fraction, ϕ_{RIGID}, and using a three-phase model:[35−45]

$$\phi_{RIGID} = \phi_C + \phi_{IMM} \tag{7a}$$

$$\phi_{RIGID} + \phi_M = 1 \tag{7b}$$

According to glass transition theory,[35−37] in a semicrystalline polymer sample, only the mobile chains contribute to the principal glass transition step, and these chains will undergo a thermal transition from the solid state below T_g to the liquid state above T_g. The heat capacity increment value at T_g can therefore be used to deduce the mobile fraction, ϕ_M, directly from

$$\phi_M = \Delta C_p^{sc}/\Delta C_{p0} \tag{8}$$

where ΔC_p^{sc} is the heat capacity increment at T_g measured for semicrystalline sample[35−45] containing the beta-pleated sheets. It should be appreciated that the heat capacity increment for the numerator of eq 8 is calculated at the glass transition temperature value for each semicrystalline sample, which value is upshifted in temperature from the T_g value of the less ordered sample, as indicated by the two downward arrows on the temperature axis in Figure 5b.

Table 2 lists the heat capacity increment, ΔC_p, mobile fraction from eq 8, total rigid fraction from eq 7b, and beta-sheet crystal content (from FTIR), for *B. mori* samples as a function of treatment. The data for the heat capacity of the semicrystalline

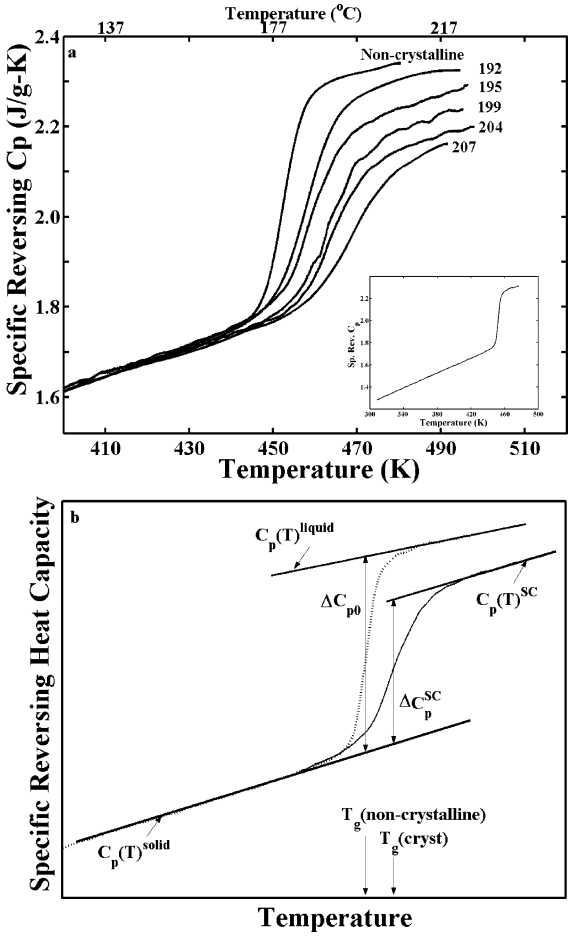

Figure 5. (a) Specific reversing heat capacity vs temperature during TMDSC scanning of *B. mori* silk fibroin at 2 °C/min. Samples were scanned prior to crystallization (marked noncrystalline) and after isothermal crystallization at the temperatures indicated. For comparison, temperatures in °C are indicated above. The inset shows the specific reversing heat capacity for one noncrystalline sample over the entire temperature range. (b) Sketch showing the method of determining the heat capacity increment at the glass transition temperature, T_g, from a plot of the specific reversing heat capacity vs temperature. Less ordered, noncrystalline fibroin: dashed curve; crystalline fibroin, containing beta-pleated sheets: light solid curve. The heavy solid lines are the tangents to the heat capacity curve at low and high temperature above T_g. From the tangents we derive the solid-state heat capacity, $C_p(T)^{solid}$, the liquid heat capacity, $C_p(T)^{liquid}$ (from the noncrystalline sample), and the semicrystalline heat capacity, $C_p(T)^{SC}$ (from a sample containing beta-pleated sheets). The increment is found from the difference of the heat capacity of the extrapolated tangents, at the location of T_g.

samples are significant to the second position past the decimal; the third digit is included only to show the variation. The error ranges listed in the table cover over the sample-to-sample variations in the heat capacity seen, for example, in Figure 5 below T_g. The close agreement between the total rigid fraction calculated from eq 7b and the crystalline fraction from FSD of the infrared spectra suggests that the crystal fraction accounts for the rigid fraction almost entirely. Any immobilized less ordered fraction, ϕ_{IMM}, is very small.

Figure 6 shows the ΔC_p increment at T_g vs beta-sheet content determined from FTIR. The filled circles are the crystalline samples containing beta-pleated sheets. Less ordered samples are shown by the empty squares. The straight solid line represents the best linear fit to experimental data, resulting in

$$\Delta C_p = 0.475 - 0.494\phi_C \tag{9}$$

with a correlation coefficient of −0.995. The dotted line in

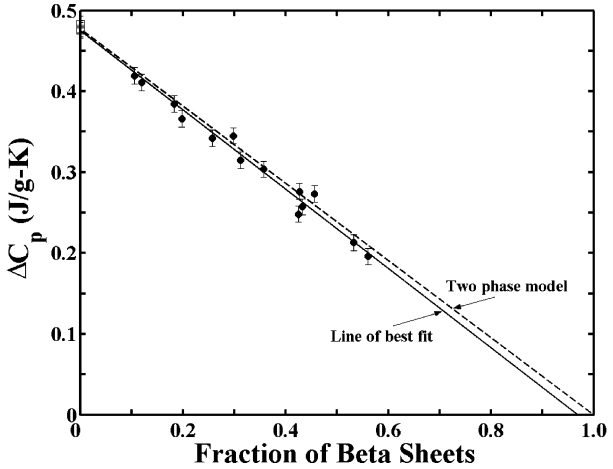

Figure 6. Specific reversing heat capacity increment, ΔC_p, vs fraction of beta-sheets, ϕ_C, determined from FTIR analysis of *B. mori* silk fibroin films: crystalline samples, filled circles; noncrystalline samples, empty squares; solid line, best fit to the data; dashed line, expected variation of ΔC_p with crystallinity using a two-phase model where $\phi_M + \phi_C = 1$ and $\phi_{IMM} = 0$.

Figure 6 represents expected results using a two-phase assumption for silk fibroin ($\phi_{IMM} = 0$). Under a two-phase assumption (beta-sheet crystals and mobile phases only) we expect that the heat capacity increment at T_g vs crystallinity would extrapolate to zero in a sample with crystal fraction of unity. Figure 6 shows that for *B. mori* silk fibroin the fitted (solid) line extrapolates to $\Delta C_p = 0$ at a beta-sheet fraction of 0.97. The deviation of the fitted line from the dotted line suggests that there could be a small amount of immobilized, but noncrystalline, chains in silk fibroin above the glass transition of the mobile phase. The amount will be very small and will be covered by the error bars in our measurement. For example, in *B. mori* silk fibroin containing 10% beta-sheets, the deviation is 0.5%. For a sample containing 60% beta-sheets, the deviation is less than 2%.

The correlation represented by eq 9 provides a method by which the beta-sheet fraction, ϕ_C, may be assessed from measurement of the heat capacity increment at the glass transition temperature. There are several advantages to this method: (1) A very small amount of sample (e.g., less than ~3 mg) can be used. (2) The technique is quantitative when the calibrations of the DSC are performed as outlined in the Experimental Section. (3) The thermal method can be used for samples that are not amenable to other types of analyses. For example, samples that cannot be cast onto salt plates, or whose surfaces are too rough for attenuated total reflectance measurements of FTIR spectra, can be analyzed thermally. Furthermore, some samples, in which the beta-sheet crystals are very tiny and not numerous, cannot readily be investigated by X-ray diffraction. The thermal heat capacity method is ideal for this type of sample.

Further work in our laboratory is underway to study the crystallization kinetics of *B. mori* silk fibroin[67] and to apply this approach using heat capacity increment to other proteins containing crystalline beta-sheets.

Conclusions

In this work, we demonstrate the use of the infrared spectroscopic technique of Fourier self-deconvolution to determine the absolute fraction of the crystalline beta-pleated sheets in silk fibroin. For samples treated isothermally at temperature from 192 to 214 °C, the beta-sheet fraction ranged from 0.11 to 0.43. Samples treated by exposure to methanol had beta-sheet fractions from 0.43 to 0.56.

A thermal method, using the specific reversing heat capacity increment, was used for the first time to quantify the mobile fraction through its relaxation behavior at the glass transition temperature. A negative linear correlation was observed between the heat capacity increment, ΔC_p, from TMDSC and the beta-sheet fraction (ϕ_C from FSD), given by $\Delta C_p = 0.475 - 0.494\phi_C$. We present this method as an attractive alternative to X-ray diffraction for the study of *B. mori* silk fibroin. Measurement of the specific reversing heat capacity increment (1) correlates with spectroscopic methods such as FTIR, (2) quantifies the beta-pleated sheet fractions including in cases where other methods, such as X-ray or FTIR, cannot be used, and (3) can serve as a standard method to assess the beta-pleated sheet fraction in this and other fibrous proteins.

Acknowledgment. The authors thank the National Science Foundation Division of Materials Research, Polymers Program, for support of this research through Grant DMR-0402849.

References and Notes

(1) McGrath, K., Kaplan, D., Eds.; *Protein-Based Materials;* Birkhauser Press: Boston, MA, 1996; pp 103−133.
(2) Ha, S. W.; Gracz, H. S.; Tonelli, A. E.; Hudson, S. M. *Biomacromolecules* **2005**, *6*, 2563.
(3) Altman, G. H.; Diaz, F.; Jakuba, C.; Calabro, T.; Horan, R. L.; Chen, J. S.; Lu, H.; Richmond, J.; Kaplan, D. L. *Biomaterials* **2003**, *24*, 401.
(4) Foo, C. W. P.; Kaplan, D. L. *Adv. Drug Delivery Rev.* **2002**, *54*, 1131.
(5) Demura, M.; Asakura, T.; Kuroo, T. *Biosensors* **1989**, *4*, 361.
(6) Kaplan, D. L., Adams, W. W., Farmer, B., Viney, C., Eds.; *Silk Polymers: Materials Science and Biotechnology*; ACS Symposium Series 544; American Chemical Society: Washington, DC, 1994.
(7) Magoshi, J.; Magoshi, Y.; Nakamura, S.; Kasai, N.; Kakudo, M. *J. Polym. Sci., Polym. Phys.* **1977**, *15*, 1675.
(8) Shen, Y.; Johnson, M. A.; Martin, D. C. *Macromolecules* **1998**, *31*, 8857.
(9) Asakura, T.; Kuzuhara, A.; Tabeta, R.; Saito, H. *Macromolecules* **1985**, *18*, 1841.
(10) Saito, H.; Tabeta, R.; Asakura, T.; Iwanaga, Y.; Shoji, A.; Ozaki, T.; Ando, I. *Macromolecules* **1984**, *17*, 1405.
(11) Ishida, M.; Asakura, T.; Yokoi, M.; Saito, H. *Macromolecules* **1990**, *23*, 88.
(12) Jin, H. J.; Kaplan, D. L. *Nature (London)* **2003**, *424*, 1057.
(13) Valluzzi, R.; Gido, S. P.; Zhang, W. P.; Muller, W. S.; Kaplan, D. L. *Macromolecules* **1996**, *29*, 8606.
(14) Valluzzi, R.; Gido, S. P. *Biopolymers* **1997**, *42*, 705.
(15) Goormaghtigh, E.; Cabiaux, V.; Ruysschaert, J. M. *Eur. J. Biochem.* **1990**, *193*, 409.
(16) Jung, C. *J. Mol. Recognit.* **2000**, *13*, 325.
(17) Dong, A.; Huang, P.; Caughey, W. S. *Biochemistry* **1990**, *29*, 3303.
(18) Mouro, C.; Jung, C.; Bondon, A.; Simonneaux, G. *Biochemistry* **1997**, *36*, 8125.
(19) Venyaminov, S. Y.; Kalnin, N. N. *Biopolymers* **1990**, *30*, 1259.
(20) Chen, X.; Knight, D. P.; Shao, Z. Z.; Vollrath, F. *Polymer* **2001**, *42*, 9969.
(21) Chen, X.; Shao, Z. Z.; Marinkovic, N. S.; Miller, L. M.; Zhou, P.; Chance, M. R. *Biophys. Chem.* **2001**, *89*, 25.
(22) Motta, A.; Fambri, L.; Migliaresi, C. *Macromol. Chem. Phys.* **2002**, *203*, 1658.
(23) Asakura, T.; Kaplan, D. L. *Silk Production and Processing*; Academic Press: New York, 1994; Vol. 4, p 1.
(24) Zhou, C. Z.; Confalonieri, F.; Medina, N.; Zivanovic, Y.; Esnault, C.; Yang, T.; Jacquet, M.; Janin, J.; Duguet, M.; Perasso, R.; Li, Z. G. *Nucleic Acids Res.* **2000**, *28*, 2413.
(25) Yao, J. M.; Nakazawa, Y.; Asakura, T. *Biomacromolecules* **2004**, *5*, 680.
(26) Agarwal, N.; Hoagland, D. A.; Farris, R. J. *J. Appl. Polym. Sci.* **1997**, *63*, 401.
(27) Tretinnikov, O. N.; Tamada, Y. *Langmuir* **2001**, *17*, 7406.
(28) Krejchi, M. T.; Cooper, S. J.; Deguchi, Y.; Atkins, E. D. T.; Fournier, M. J.; Mason, T. L.; Tirrell, D. A. *Macromolecules* **1997**, *30*, 5012.
(29) Asakura, T.; Ohgo, K.; Komatsu, K.; Kanenari, M.; Okuyama, K. *Macromolecules* **2005**, *38*, 7397.
(30) Yamane, T.; Umemura, K.; Nakazawa, Y.; Asakura, T. *Macromolecules* **2003**, *36*, 6766.
(31) Taddei, P.; Monti, P. *Biopolymers* **2005**, *78*, 249.
(32) Warwicker, J. O. *J. Mol. Biol.* **1960**, *2*, 350.

(33) Um, I. C.; Kweon, H. Y.; Park, Y. H.; Hudson, S. *Int. J. Biol. Macromol.* **2001**, *29*, 91.
(34) Teramoto, H.; Miyazawa, M. *Biomacromolecules* **2005**, *6*, 2049.
(35) Lau, S. F.; Suzuki, H.; Wunderlich, B. *J. Polym. Sci., Polym. Phys.* **1984**, *22*, 379.
(36) Grebowicz, J.; Lau, S. F.; Wunderlich, B. *J. Polym. Sci., Polym. Symp.* **1984**, *71*, 19.
(37) Suzuki, H.; Grebowicz, J.; Wunderlich, B. *Makromol. Chem., Macromol. Chem. Phys.* **1985**, *186*, 1109.
(38) Huo, P. P.; Cebe, P. *Macromolecules* **1992**, *25*, 902.
(39) Cebe, P.; Huo, P. P. *Thermochim. Acta* **1994**, *238*, 229.
(40) Cheng, S. Z. D.; Cao, M. Y.; Wunderlich, B. *Macromolecules* **1986**, *19*, 1868.
(41) Xu, H.; Ince, B. S.; Cebe, P. *J. Polym. Sci., Polym. Phys.* **2003**, *41*, 3026.
(42) Xu, H.; Cebe, P. *Macromolecules* **2005**, *38*, 770.
(43) Xu, H.; Cebe, P. *Macromolecules* **2004**, *37*, 2797.
(44) Huo, P.; Cebe, P. *Colloid Polym. Sci.* **1992**, *270*, 840.
(45) Lu, S. X.; Cebe, P. *Polymer* **1996**, *37*, 4857.
(46) Di Lorenzo, M. L.; Zhang, G.; Pyda, M.; Lebedev, B. V.; Wunderlich, B. *J. Polym. Sci., Polym. Phys.* **1999**, *37*, 2093.
(47) Wunderlich, B.; Jin, Y. M.; Boller, A. *Thermochim. Acta* **1994**, *238*, 277.
(48) Boller, A.; Okazaki, I.; Ishikiriyama, K.; Zhang, G.; Wunderlich, B. *J. Therm. Anal.* **1997**, *49*, 1081.
(49) Pyda, M.; Boller, A.; Grebowicz, J.; Chuah, H.; Lebedev, B. V.; Wunderlich, B. *J. Polym. Sci., Polym. Phys.* **1998**, *36*, 2499.
(50) Ishikiriyama, K.; Wunderlich, B. *J. Therm. Anal.* **1997**, *50*, 337.
(51) Kauppinen, J. K.; Moffatt, D. J.; Mantsch, H. H.; Cameron, D. G. *Appl. Spectrosc.* **1981**, *35*, 271.
(52) Rahmelow, K.; Hubner, W. *Appl. Spectrosc.* **1996**, *50*, 795.
(53) Lorenz-Fonfria, V. A.; Padros, E. *Spectrochim. Acta, Part A: Mol. Biomol. Spectrosc.* **2004**, *60*, 2703.
(54) Lorenz-Fonfria, V. A.; Villaverde, J.; Padros, E. *Appl. Spectrosc.* **2002**, *56*, 232.
(55) Skrovanek, D. J.; Howe, S. E.; Painter, P. C.; Coleman, M. M. *Macromolecules* **1985**, *18*, 1676.
(56) Coleman, M. M.; Lee, K. H.; Skrovanek, D. J.; Painter, P. C. *Macromolecules* **1986**, *19*, 2149.
(57) Skrovanek, D. J.; Painter, P. C.; Coleman, M. M. *Macromolecules* **1986**, *19*, 699.
(58) Meng, G. T.; Ma, C. Y. *Int. J. Biol. Macromol.* **2001**, *29*, 287.
(59) van de Weert, M.; Haris, P. I.; Hennink, W. E.; Crommelin, D. J. A. *Anal. Biochem.* **2001**, *297*, 160.
(60) Wilson, D.; Valluzzi, R.; Kaplan, D. *Biophys. J.* **2000**, *78*, 2690.
(61) Barth, A. *Prog. Biophys. Mol. Biol.* **2000**, *74*, 141.
(62) Arrondo, J. L. R.; Muga, A.; Castresana, J.; Goni, F. M. *Prog. Biophys. Mol. Biol.* **1993**, *59*, 23.
(63) Casal, H. L.; Kohler, U.; Mantsch, H. H. *Biochim. Biophys. Acta* **1988**, *957*, 11.
(64) Byler, D. M.; Susi, H. *Biopolymers* **1986**, *25*, 469.
(65) Lazo, N. D.; Downing, D. T. *Macromolecules* **1999**, *32*, 4700.
(66) Khurana, R.; Fink, A. L. *Biophys. J.* **2000**, *78*, 994.
(67) Hu, X.; Cebe, P. *Am. Chem. Soc. Div. Polym. Mater.: Sci. Eng. Prepr.* **2005**, *93*, 652−653.

MA0610109